JOURNAL OF CATALYSIS **162,** 76–87 (1996)
ARTICLE NO. 0261

Molybdenum Nitride and Carbide Prepared from Heteropolyacids

1. Preparation and Characterization

Senzi Li and Jae Sung Lee[1]

Department of Chemical Engineering, Pohang University of Science and Technology, San 31, Hyoja-dong, Pohang, 790-784 Korea

Received November 9, 1995; revised March 13, 1996; accepted March 25, 1996

Molybdenum nitride and carbide containing phosphorus were prepared by temperature programmed reaction (TPR) of 12-molybdophosphoric acid, a Keggin-type heteropolyacid (HPA), with NH_3 and CH_4/H_2. The process of solid transformation and the properties of prepared materials were compared with those of nitride and carbide made from MoO_3. Product phases were produced at much lower temperature from HPA, and smaller crystallite sizes were obtained. Yet, HPA-derived materials showed lower surface areas and CO chemisorption probably because phosphorus remaining in the products blocked their pores and adsorption sites. Since the involved solid transformations were topotactic, two precursors yielded products with completely different morphology of the particles. The distribution of phosphorus in HPA-derived Mo_2N was highly uniform. © 1996 Academic Press, Inc.

INTRODUCTION

Molybdenum and tungsten carbides and nitrides are active catalysts for a range of reactions typically occurring on noble metals such as hydrogenation of CO and olefins (1–7), NH_3 synthesis (8), and hydrocarbon reforming (9), and hydrogenolysis of hydrocarbons (10, 11). Importantly, the activity of CO hydrogenation (12) and alkane hydrogenolysis (11) over Mo_2C was reported to be similar to that of ruthenium and the behavior of hydrocarbon isomerization over WC resembled that of platinum (13). These results inspired many studies which were aimed at employing these materials as a potential substitute for noble metals as catalysts.

In order to use metal carbides or nitrides as catalysts, they must be prepared with desirable physical properties. The past decade has seen significant progress made in both synthesis and characterization of these materials (14). For example, Mo_2N with a specific surface area (S_g) as high as 220 $m^2\ g^{-1}$ has been synthesized by a slow temperature-programmed reaction (TPR) between MoO_3 and NH_3 (15). The subsequent carburization of Mo_2N to α-MoC_{1-x} by TPR with a CH_4/H_2 mixture gave nearly the same high surface area (16, 17).

[1] To whom correspondence should be addressed.

Most of the reported synthesis of molybdenum nitride and carbide involved MoO_3 as a precursor. It was demonstrated that the solid transformation of molybdenum oxide to nitride and subsequently to carbide was topotactic (17, 18) under some favorable preparation conditions that yielded carbide and nitride products with high specific surface areas. Thus, the structure and texture of the resulting nitride and carbide were governed by those of the precursor MoO_3. When usual MoO_3 powders with a highly anisotropic platelet shape were employed, the morphology was preserved in Mo_2N and α-MoC_{1-x} as a consequence of the pseudomorphism, a signature of the topotactic solid transformation (17, 18). In search of precursors with a morphology different from that of MoO_3, we used a heteropolyacid (HPA), 12-molybdophosphoric acid, as a precursor in the synthesis of molybdenum carbides or nitrides in order to evaluate the potential of the alternative synthetic method and to investigate the transformation process. Special attention was also paid to the behavior of phosphorus during the transformation and in the soild products. Phosphorus is a well known catalyst poison in many reactions catalyzed by transition metals. Recently, however, its promotional effects have been reported in the hydrodenitrogenation and hydrodesulfurization over molybdenum-based catalysts (19–21). We employed several techniques such as thermogravimetric analysis (TGA), temperature-programmed reaction (TPR), X-ray diffraction (XRD), infrared spectroscopy (IR), X-ray photoelectron spectroscopy (XPS), scanning electron microscopy (SEM), energy-dispersive X-ray spectroscopy (EDS), electron probe microanalysis (EPMA), and CO chemisorption to investigate the structure and its evolution during the synthesis reaction.

EXPERIMENTAL

Temperature Programmed Reaction

Molybdenum nitride and carbide were prepared by the TPR method described in detail elsewhere (17, 21). Typically, 1 g of precursor, $H_3PMo_{12}O_{40} \cdot 26H_2O$ (Junsei, 99.95%), denoted as HPA throughout this paper, MoO_3

0021-9517/96 $18.00

powder (Aldrich, 99.95%); or a physical mixture (ground with a mortar and a pestle) of MoO_3 and P_2O_5 (Janssen, 99%), denoted as $MoO_3 + P_2O_5$, was loaded in a U-shaped quartz reaction cell stuffed with quartz wool at the bottom to hold the powders. All materials were synthesized at atmospheric pressure. A stream of NH_3 (Matheson, 99.99%) was passed through the reactor cell at a rate of 110 μmol s^{-1}. Following rapid heating to 500 K, the samples were further heated to the indicated temperatures by TPR with a linear ramping rate of 30 K h^{-1}. The same procedure was employed for carbide preparation with a stream of $CH_4/4H_2$ instead of NH_3.

In order to monitor gas evolution during the synthesis, effluent gases were analyzed by a Hewlett Packard 5890A gas chromatograph (GC) equipped with a thermal conductivity detector (TCD). A 1 m long, 1/8 inch diameter stainless steel tube packed with Porapak N or Q (Altech) was used as a column material for product analysis of NH_3 TPR or CH_4/H_2 TPR, respectively. Sample injection to GC was performed every 5 min by a six-port sampling valve attached on the stream line.

Methods of Characterization

Powder X-ray diffraction (XRD) measurements were conducted using a Rigaku Dmax-B diffractometer with Cu$K\alpha$ radiation. For each sample, TPR was stopped at the indicated temperature and the reactor was quenched to room temperature (RT). Since fresh molybdenum carbide and nitride burned violently with flame upon exposure to air ("pyrophorbic"), the samples were passivated prior to the XRD measurements by letting air diffuse slowly into the reaction cell with one end of the reactor open to atmosphere for 10 h.

The thermogravimetric analysis was carried out under a N_2 atmosphere on a Perkin–Elmer TGS-2. The temperature range for analysis was from 350 to 1100 K with a heating rate of 10 K min^{-1}. The morphology of passivated samples was observed by scanning electron microscopy on a Jeol JSM-840A. The lateral distribution of P was determined by electron probe microanalysis and its concentration by energy-dispersive X-ray spectroscopy, both on a Jeol JXA-8600. For these analyses, samples were mounted on graphite stubs and gold was sputtered onto them to ensure adequate conductivity. X-ray photoelectron spectroscopy measurements were conducted for passivated samples with a Perkin–Elmer PHI 5400 ESCA spectrometer with monochromatic Mg$K\alpha$ radiation (1253.6 eV) and the analyzer pass energy of 89.45 eV. Binding energies were corrected for surface charging by referencing them to the energy of C 1*s* peak of contaminant carbon at 285.0 eV. Infrared (IR) spectra were recorded with a Perkin–Elmer 1800 FT–IR double beam spectrophotometer on KBr pellets containing ca. 1 wt% of HPA sample powders. All spectra were the averages of 16 individual scans measured at RT with an instrumental resolution of 4.0 cm^{-1}.

The amount of P contained in the Mo_2N sample was determined by a precipitation method after converting it to $(NH_4)_3PMo_{12}O_{40}$ (23). About 0.5 g of Mo_2N, produced from TPR of HPA with NH_3, was dissolved in 50 ml of concentrated HNO_3 at 330 K during stirring until all the solid vanished and a clear yellow-green solution was obtained. Yellowish $(NH_4)_3PMo_{12}O_{40} \cdot nH_2O$ precipitate was formed by the addition of 200 ml of 2% NH_4NO_3 solution. The resulting precipitate was allowed to settle overnight before filtering. The filtrated precipitate was calcined in the oven at 573 K for 4 h and cooled naturally in a desiccator before weighing. XRD and IR were employed to determine the structure and the composition of the precipitate. Both techniques indicated that only $(NH_4)_3PMo_{12}O_{40}$ was produced.

The specific surface areas S_g of the samples were determined on a constant volume adsorption apparatus (Chemisorb 102, Micrometrics) by the N_2 BET method. Chemisorption of CO was measured at RT in the same apparatus. After preparation, the sample was cooled to 570 K and treated with H_2 for 0.2 h, evacuated at this temperature for 0.5 h to 5×10^{-3} Pa, and then cooled to RT. An initial isotherm was taken to measure total CO uptake. Then the sample was evacuated at RT for 0.5 h and a second isotherm was obtained to measure weakly adsorbed CO. The isotherms were extrapolated to zero pressure and the difference in CO uptake at that pressure was taken as the amount of CO chemisorbed irreversibly. The surface site density was calculated as the molecules of CO uptake per unit surface area.

RESULTS

Decomposition of HPA

The TGA of $H_3PMo_{12}O_{40} \cdot 26H_2O$ shown in Fig. 1 indicated that the decomposition of the HPA involved three

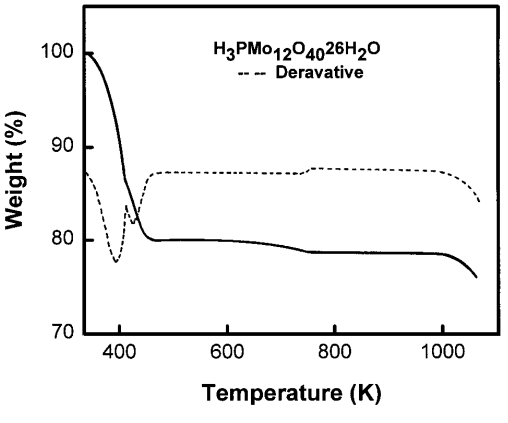

FIG. 1. Thermal gravimetric analysis (TGA) profile of $H_3PMo_{12}O_{40} \cdot 26H_2O$ under N_2 flow with a heating rate of 10 K min^{-1}.

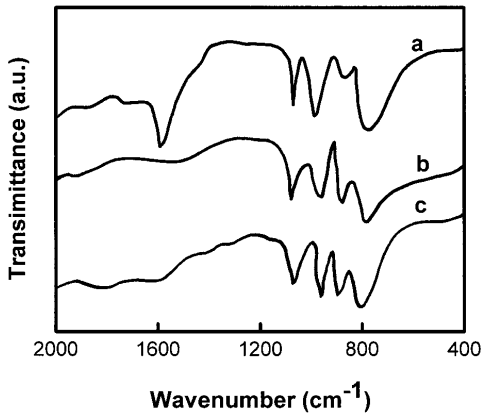

FIG. 2. Infrared (IR) spectra of heteropolyacids: (a) fresh $H_3PMo_{12}O_{40} \cdot 26H_2O$, (b) dehydrated at 450 K for 10 h under He flow, (c) dehydrated at 450 K for 10 h under CH_4/H_2 flow.

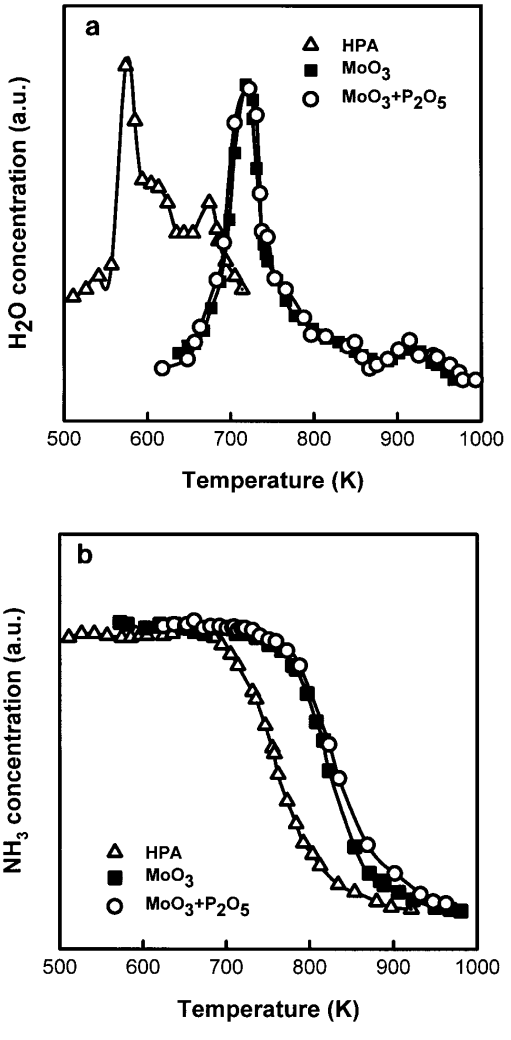

FIG. 3 Temperature-programmed reaction (TPR) profiles of various precursors with NH_3: (a) water formation and (b) NH_3 decomposition. NH_3 flow rate is 110 μmol s^{-1}; heating rate is 30 K h^{-1}.

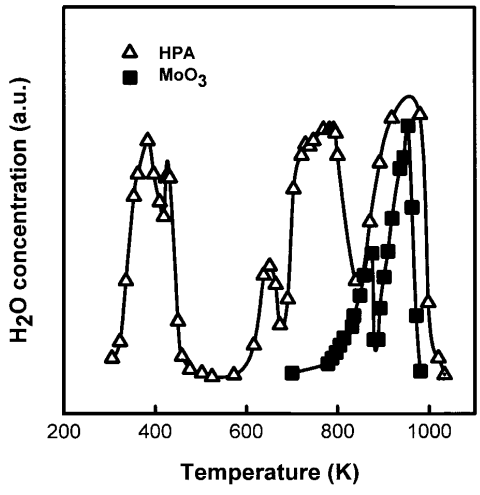

FIG. 4. Temperature-programmed reaction (TPR) profiles of different precursors with $CH_4/4H_2$: gas flow rate is 110 μmol s^{-1}, heating rate is 30 K h^{-1}.

stages. At the temperature range from 330 to 410 K, some of the water molecules were removed. Most of the water molecules were removed in the subsequent second stage occurring between 410 and 480 K. Infrared spectra of HPA are compared in Fig. 2. In Fig. 2a, fresh $H_3PMo_{12}O_{40} \cdot 26H_2O$ showed four peaks at 600–1100 cm^{-1} and a broad peak around 1600 cm^{-1}. The four peaks are characteristic of Keggin structure of HPA and assigned to (from lower wave number peaks) two bands due to Mo–O–Mo bridging bonds, a band due to Mo=O bond stretching, and a band due to P–O bond stretching (24). Upon dehydration at 450 K for 10 h under He (Fig. 2b) or CH_4/H_2 flow (Fig. 2c), the peak due to water disappeared, but the four peaks remained unchanged. Hence, it was concluded that the primary structure of $H_3PMo_{12}O_{40}$ was preserved during these dehydration processes. At the third stage (480–750 K), HPA was finally decomposed to crystalline MoO_3 and amorphous P_2O_5 as seen by IR and XRD. The overall decomposition process can be summarized as follows:

$$H_3PMo_{12}O_{40} \cdot 26H_2O \xrightarrow[330\text{–}410\ K]{\text{First stage}} H_3PMo_{12}O_{40} \cdot 16H_2O$$
$$\xrightarrow[410\text{–}480\ K]{\text{Second stage}} H_3PMo_{12}O_{40} \xrightarrow[480\text{–}750\ K]{\text{Third stage}} P_2O_5 + MoO_3. \quad [1]$$

The number of water molecules retained in the HPA after each stage was estimated from the weight change.

Temperature-Programmed Reaction

When a stream of NH_3 was passed at RT through the reactor in which HPA was loaded, a great amount of H_2O was formed. The process proceeded so rapidly below 500 K that it could not be traced by GC simultaneously. Hence,

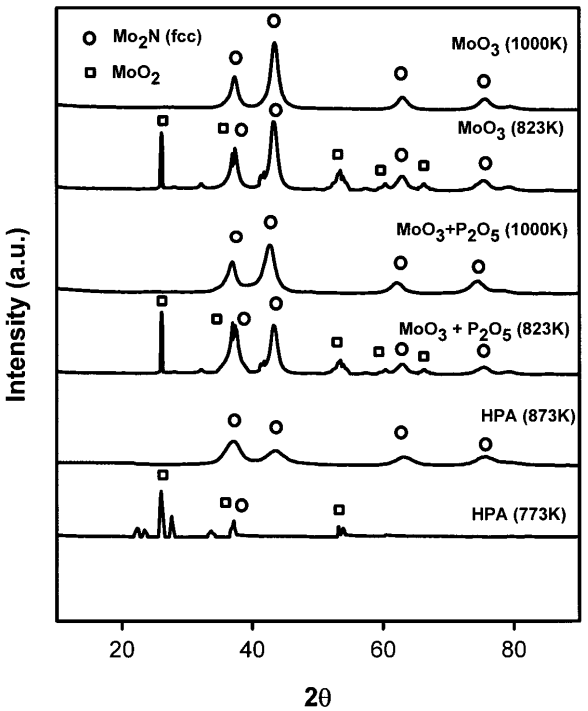

FIG. 5. X-ray diffraction patterns for samples prepared from different precursors and at different terminal temperatures of TPR with NH_3.

after all the initially formed water was carried away by NH_3, the temperature program was initiated from 500 K.

The gas phase concentrations of H_2O, NH_3, and N_2 were monitored by GC during TPR and are shown in Fig. 3 for H_2O and NH_3. The trace for N_2 formation followed exactly the trace for NH_3 disappearance, and thus is not shown. It was evident that MoO_3 and $MoO_3 + P_2O_5$ followed almost the same reduction route. However, the whole process of molybdenum nitride formation from HPA was shifted to lower temperatures by about 150 K.

TABLE 1

Physical Properties of Mo_2N Powders Prepared from Different Precursors

Precursor	MoO_3	$(MoO_3 + P_2O_5)$	$H_3PMo_{12}O_{40} \cdot 26H_2O$
$S_g/m^2\ g^{-1}$	175	131	48
D_c[a]/nm	5.9	5.4	3.4
CO chemisorption/μmol g^{-1}			
Total	557.8	59.2	7.5
Irreversible	413.8	50.0	6.4
Site density/10^{14} cm^{-2}			
Total	2.11	0.30	0.10
Irreversible	1.56	0.25	0.09

[a] Crystal size calculated from X-ray line broadening. $D_c = \lambda/\beta \cos\theta$, where λ is the wavelength of Cu$K\alpha$ X-ray radiation, θ is the Bragg angle, and β is the half-width corrected for $K\alpha$ doublet separation and instrumental broadening.

TABLE 2

Relative Intensity of XRD Peaks of Mo_2N Prepared from Different Precursors

Precursor	(111)	(200)	(220)	(311)	(222)
MoO_3	28	100	11	9	2
$(MoO_3 + P_2O_5)$	61	100	18	11	4
$H_3PMo_{12}O_{40} \cdot 26H_2O$	100	21	10	19	1

When the reducing gas was switched to CH_4/H_2 from NH_3, the TPR traces of water formation shown in Fig. 4 were obtained. Now the dehydration process below 500 K was much slower and was able to be followed by GC analysis. Dehydration proceeded the same way as in TGA experiments below 700 K indicating that the CH_4/H_2 gas mixture was none other than a carrier gas of H_2O under this condition. This was also supported by the IR spectrum shown in Fig. 2c. Above 700 K, HPA underwent reduction and carburization by CH_4/H_2. At first, it was reduced to MoO_2 at 700–800 K as confirmed by XRD, and then carburized to Mo_2C in the temperature range 800–1000 K. Again, reduction of HPA proceeded at much lower temperatures than that required for the reduction of MoO_3.

The structural evolution of solids during TPR was monitored by interruption of TPR at several intermediate temperatures and subsequent XRD analysis. In NH_3 TPR, MoO_2 and other unidentified intermediate phases were observed during the transformation although Mo_2N was prepared at the end of TPR regardless of the precursors. A new phase appeared before another phase vanished completely. It was observed that reduction and nitridation took place simultaneously. A few XRD patterns were shown in Fig. 5. The pure Mo_2N phase was observed below 873 K when prepared from HPA, while with MoO_3 or $MoO_3 + P_2O_5$, the pure Mo_2N phase appeared towards the end of the TPR (1000 K).

Characteristics of Mo_2N and Mo_2C Products

Specific surface areas (S_g) of precursors MoO_3 and $H_3PMo_{12}O_{40} \cdot 26H_2O$ were close to 1 $m^2\ g^{-1}$. Some prop-

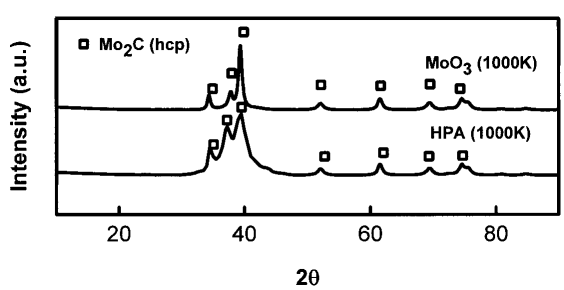

FIG. 6. X-ray diffraction patterns of Mo_2C prepared from MoO_3 and HPA by TPR with $CH_4/4H_2$. All peaks could be assigned to βMo_2C with a hexagonal close-packed structure.

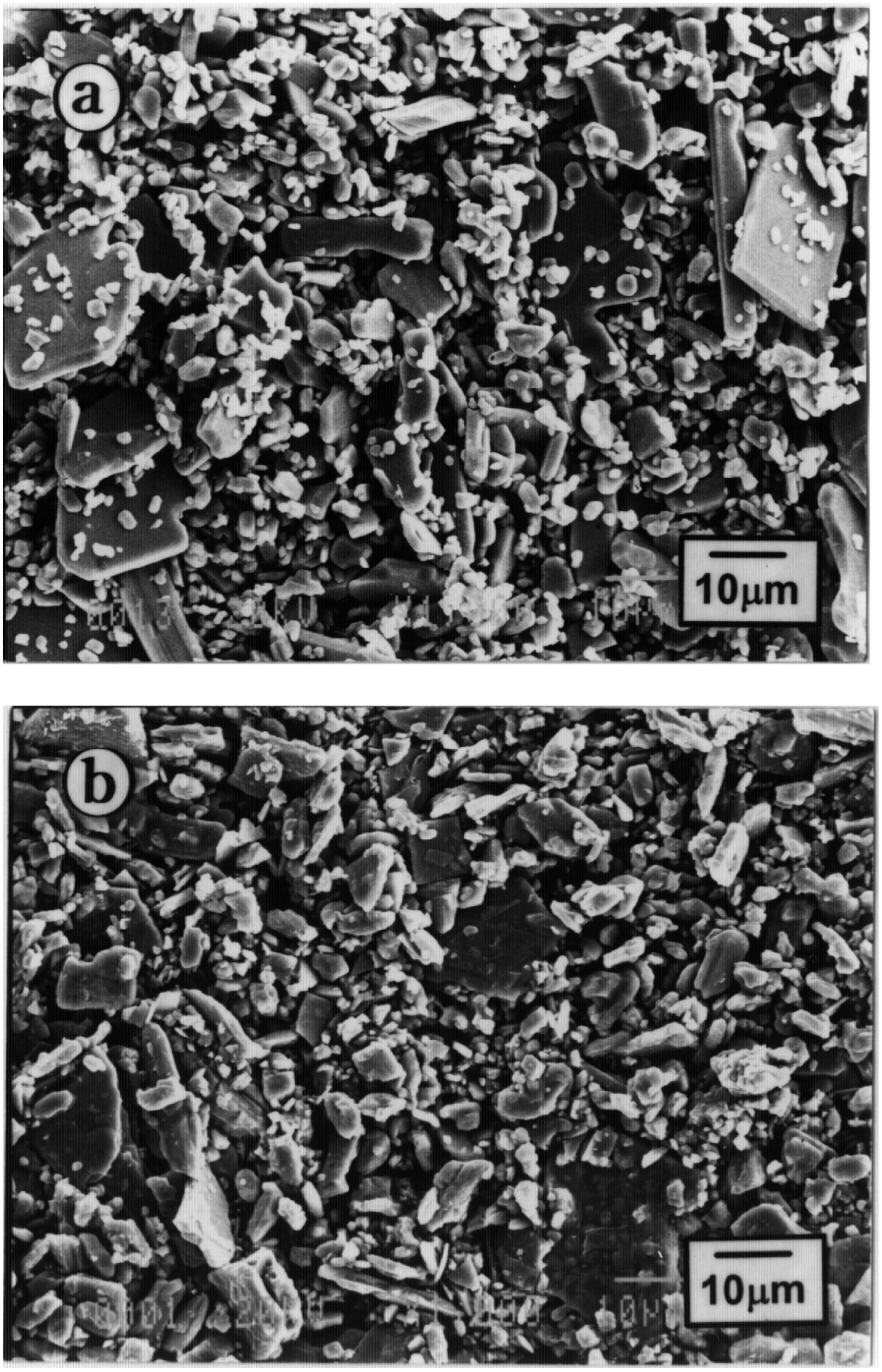

FIG. 7. Scanning electron micrographs showing pseudomorphism in the topotactic transformation of MoO_3 to Mo_2N: (a) precursor MoO_3, (b) Mo_2N prepared from MoO_3 alone, and (c) Mo_2N prepared from $MoO_3 + P_2O_5$.

erties of Mo_2N produced from three precursors under the same conditions are compared in Table 1. Mo_2N produced from MoO_3 gave the highest surface area, followed by that from $MoO_3 + P_2O_5$, and finally Mo_2N produced from HPA showed the lowest surface area. However, the crystallite sizes determined from X-ray line broadening showed a different trend. Mo_2N produced from MoO_3 and $MoO_3 + P_2O_5$ gave almost the same crystallite sizes, indicating that the mechanically mixed P_2O_5 did not interfere with the process of Mo_2N crystal formation. Mo_2N prepared from HPA appeared to form much smaller crystallites in spite of its smaller surface area. The amounts of CO adsorbed on the catalysts decreased sharply as the precursor was changed from MoO_3 to $MoO_3 + P_2O_5$, and then to

FIG. 7—*Continued*

HPA. Naturally, much smaller CO site densities were calculated when precursors contained P. Another interesting difference was observed in the relative intensity of XRD peaks of Mo_2N prepared from different precursors. As shown in Table 2, the highest intensity peak in XRD of Mo_2N produced from MoO_3 or $MoO_3 + P_2O_5$ was that of the (200) plane, while XRD of HPA-derived Mo_2N showed the highest intensity in the (111) peak. In case of Mo_2C, the XRD pattern showed that Mo_2C was produced from both HPA and MoO_3 at the end of the TPR. However, as shown in Fig. 6, Mo_2C from HPA gave much broader XRD peaks, indicating much smaller crystal sizes.

The morphology of solids was observed by SEM. As shown in Fig. 7, MoO_3 assumed a highly anisotropic platelet shape. There was no apparent change of this morphology when Mo_2N was produced from this MoO_3 in the presence or absence of P_2O_5. The SEM images of HPA and the Mo_2N produced from it are shown in Fig. 8. It is clear that a Mo_2N with a completely different morphology has been produced.

In order to see the lateral distribution of P over Mo_2N, EPMA was employed. The technique uses a focused beam of electrons to scan the sample laterally and to excite characteristic X-rays within the top 1–4 μm layer of the sample. The so-called "X-ray maps" with corresponding SEM micrographs are shown in Figs. 9 and 10. The morphologies of particles directly seen by SEM (Figs. 9a and 10a) and defined by distribution of Mo (Figs. 9b and 10b) or P (Figs. 9c and 10c) are consistent with one another. This indicates a uniform distribution of P over Mo_2N particles. This is particularly true for Mo_2N produced from HPA. The intensity of white spots in Fig. 9c representing the relative concentration of P over Mo_2N prepared from $MoO_3 + P_2O_5$ was not as homogeneous as that in Fig. 10c. Furthermore, EPMA analysis for some other areas of this Mo_2N indicated the presence of the agglomerates of a P compound. Thus it is concluded that Mo_2N produced from HPA has achieved a more uniform P distribution than Mo_2N produced from $MoO_3 + P_2O_5$.

Figure 11 shows XPS spectra of P contained in HPA precursor and Mo_2N. The curve fitting of the spectra indicated that there were two kinds of P species with binding energies of 133.5–133.8 eV and 135.2 eV. The dominant species (>85%) at 133.5–133.8 eV could be assigned to P bonded to Mo and the one at 135.2 eV assigned to P bonded to oxygen (25). Thus there seems to be little change in the chemical environment of P in precursor HPA and in Mo_2N. Furthermore, P_2O_5, initially mixed mechanically with MoO_3, has not only dispersed itself fairly uniformly on to Mo_2N particles but also has associated chemically with Mo_2N during the synthesis.

The results of quantitative analysis for P are summarized in Table 3. Chemical analysis of P contained in HPA-derived Mo_2N indicates that there was no significant loss of P during the nitride synthesis. P contents of HPA and nitride expressed in P/Mo atom ratio are almost the same and close to theoretical values for $H_2PMo_{12}O_{40}$, i.e., 1/12. Note that the same amount of P was added to $MoO_3 + P_2O_5$. Comparison of these values of bulk composition with those of XPS (probing depth ca. 2–4 nm) and EDS (probing depth

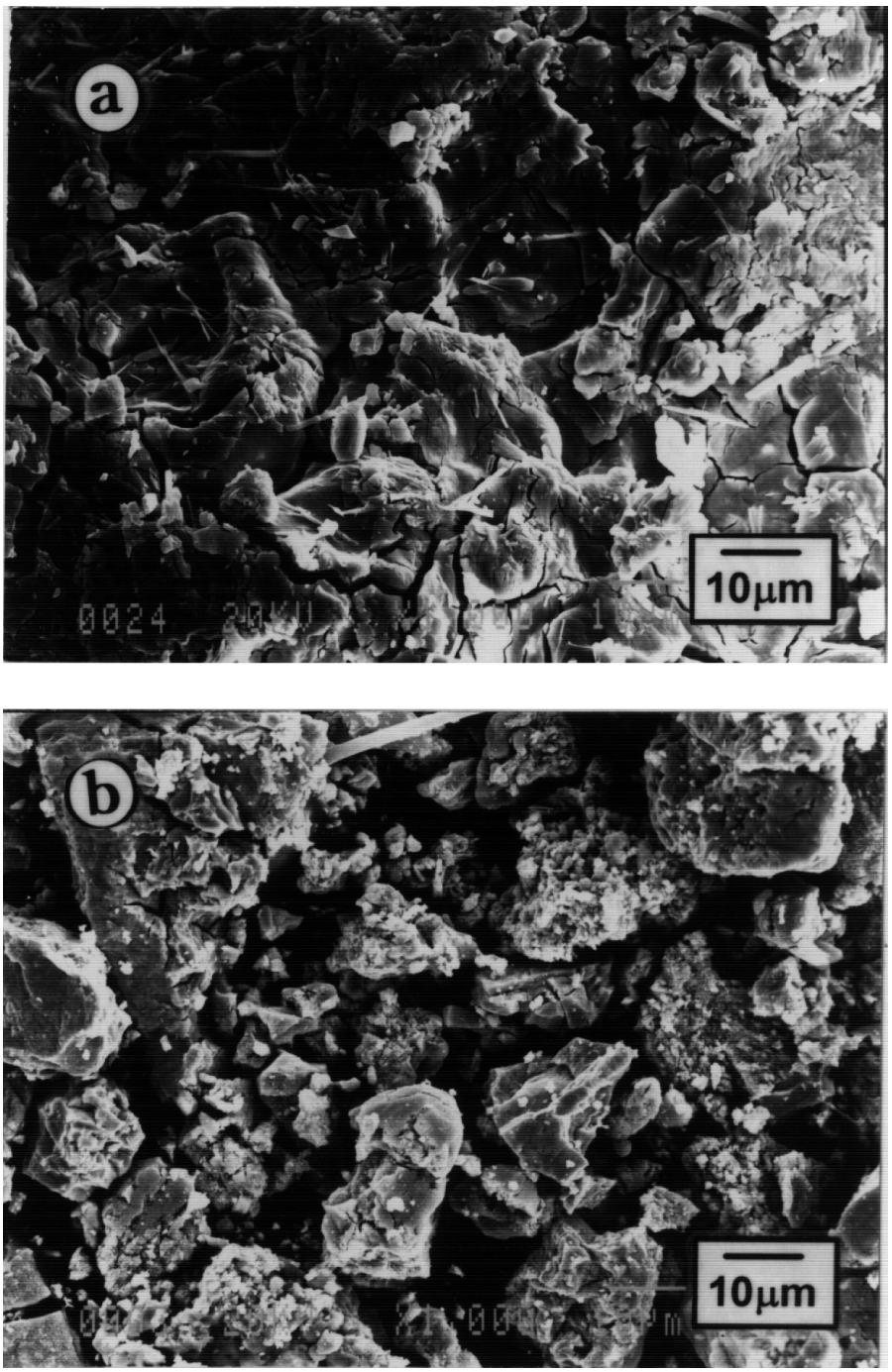

FIG. 8. Scanning electron micrographs showing morphology of (a) precursor $H_3PMo_{12}O_{40} \cdot 26H_2O$ and (b) Mo_2N prepared from it.

1–4 μm) gives an idea of the distribution of P along the depth of the sample particles. Mo_2N produced from two precursors showed similar values of P content by EDS, yet substantially different values by XPS. The XPS-measured P content for HPA-derived Mo_2N was less than that for $MoO_3 + P_2O_5$, and was the same as that for the HPA precursor. Thus it appears that P distribution in HPA and Mo_2N produced from HPA is similar and that surface concentration of P is higher for Mo_2N produced from $MoO_3 + P_2O_5$ than for that produced from HPA.

DISCUSSION

As mentioned, the most important objective of the present work was to prepare Mo_2N with a morphology different from that produced from MoO_3. This has been

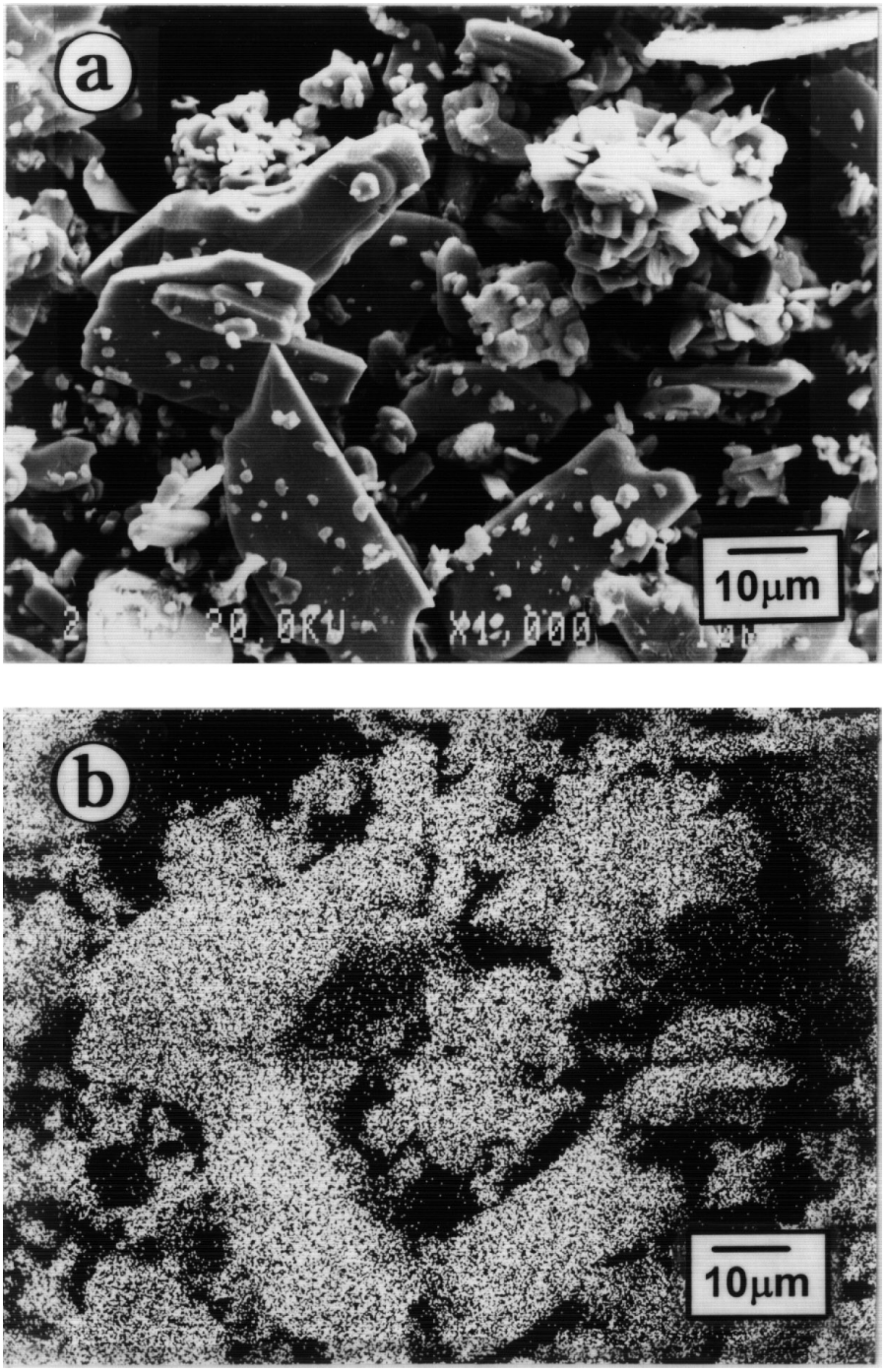

FIG. 9. Electron probe microanalysis of Mo_2N prepared from $MoO_3 + P_2O_5$: (a) SEM image of the area analyzed, (b) Mo distribution, and (c) P distribution.

achieved as can be seen in Figs. 7 and 8. Well developed MoO_3 crystals with sizes greater than 10 μm assume a highly nonisotropic platelet shape, exposing the extended (010) plane of the orthorhombic unit cell. This same morphology is also observed for the product Mo_2N. Because Mo_2N possesses the specific surface area S_g of 175 $m^2\ g^{-1}$, its particle size d_p should be ca. 3.6 nm according to the equation of $d_p = 6/S_g \cdot \rho$ where ρ is the solid density. Thus the platelets seen in Figs. 7b and 7c must be agglomerates of many small Mo_2N particles.

The reason why the morphology of the product Mo_2N is inherited from the precursor MoO_3 is that the solid transformation of MoO_3 to Mo_2N is topotactic. Pseudomorphism is a common feature of the topotactic transformation (18).

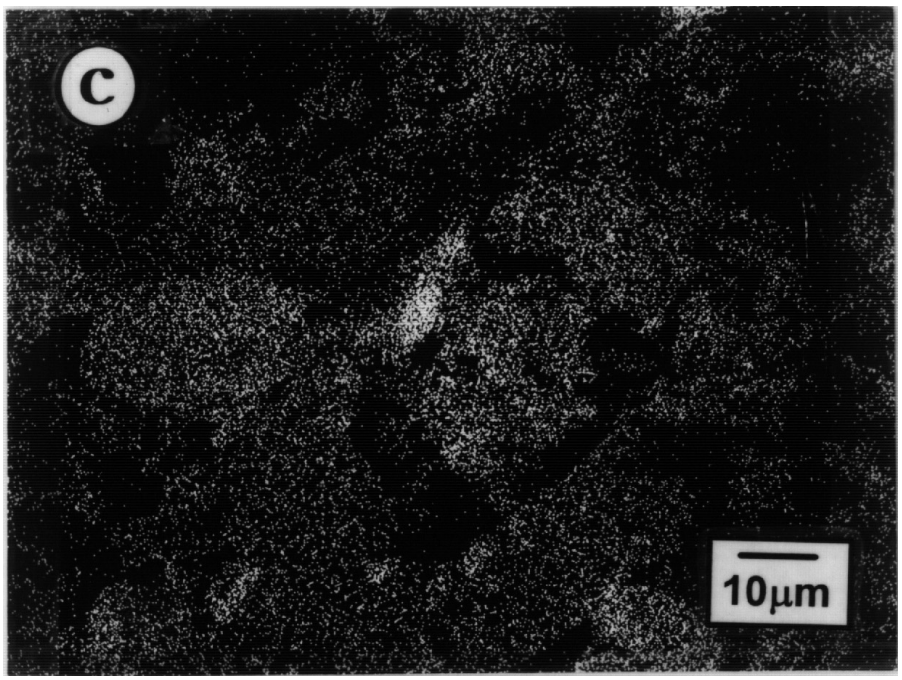

FIG. 9—*Continued*

The details of the process involved in the MoO_3-to-Mo_2N solid transformation have been studied with XRD and SEM (16, 17). The transformation involves two intermediates, MoO_2 and an unidentified phase with a composition of MoO_xN_y. Only the latter with broad XRD peaks due to a low crystallinity was proposed to be responsible for the topotactic transformation. MoO_2 is an impurity phase although it is eventually converted to Mo_2N. Our XRD results shown in Fig. 5 are consistent with the previous works.

Another evidence of topotaxy of MoO_3-to-Mo_2N transformation could be found in the relative intensity of XRD peaks of Mo_2N derived from different precursors, as shown in Table 2. Mo_2N produced from HPA shows the intensity distribution which is very close to the theoretical intensity distribution of ideal face-centered cubic crystal powders (26). This indicates that this sample assumes a random isotropic morphology. The abnormally high (200) peak in MoO_3-derived Mo_2N represents its unusual anisotropic morphology.

The primary structure of heteropolyacid $H_3PMo_{12}O_{40} \cdot 26H_2O$ has the Keggin structure with $12MoO_6$ (4 X Mo_3O_{18}) surrounding a PO_4 tetrahedron, while the secondary structure varies greatly from the perfect crystal due to the variety in the number of molecules of water of crystallization (24). In addition, the surface area of heteropolyacid was sensitive to the extent of dehydration (24). Indeed, we found that the S_g of HPA becomes 1–15 m^2 g^{-1} after dehydration depending on the dehydration conditions. Compared with N_2 (used in TGA experiments) or CH_4/H_2, ammonia is unusual in that it causes the reduction of HPA at low temperatures in addition to dehydration. Thus early stages of TPR with NH_3 proceed much faster than with CH_4/H_2. When different precursors are compared, reduction takes place at a much lower temperature for HPA than for MoO_3 with both NH_3 and CH_4/H_2. The nitride phase is formed at much lower temperatures (at least by 150 K) for HPA as shown in Fig. 5. Although the decomposition of HPA under N_2 eventually leads to MoO_3, the reduction process with NH_3 starts before complete dehydration. Even with CH_4/H_2, reduction seems to start before large MoO_3 particles are formed. Thus, the ease of removing oxygen from the loose HPA structure or incompletely developed molybdenum oxide lattice seems to be responsible for the low temperature reduction of HPA. Indeed, it has been demonstrated that the rate of MoO_3 reduction is limited by the diffusion of oxygen from the oxide lattice (14).

It is interesting to note that water formation during reduction (Fig. 3a) starts before ammonia decomposition to

TABLE 3

Quantitative Analysis of P (P/Mo Atom Ratio)

Sample	XPS[a]	EDS[b]	Chemical analysis
Precursor $H_3PMo_{12}O_{40} \cdot 26H_2O$	0.015	—	0.083
Mo_2N from $H_3PMo_{12}O_{40} \cdot 26H_2O$	0.015	0.044	0.080
Mo_2N from ($MoO_3 + P_2O_5$)	0.027	0.039	

[a] By X-ray photoelectron spectroscopy.
[b] By X-ray energy dispersive spectroscopy.

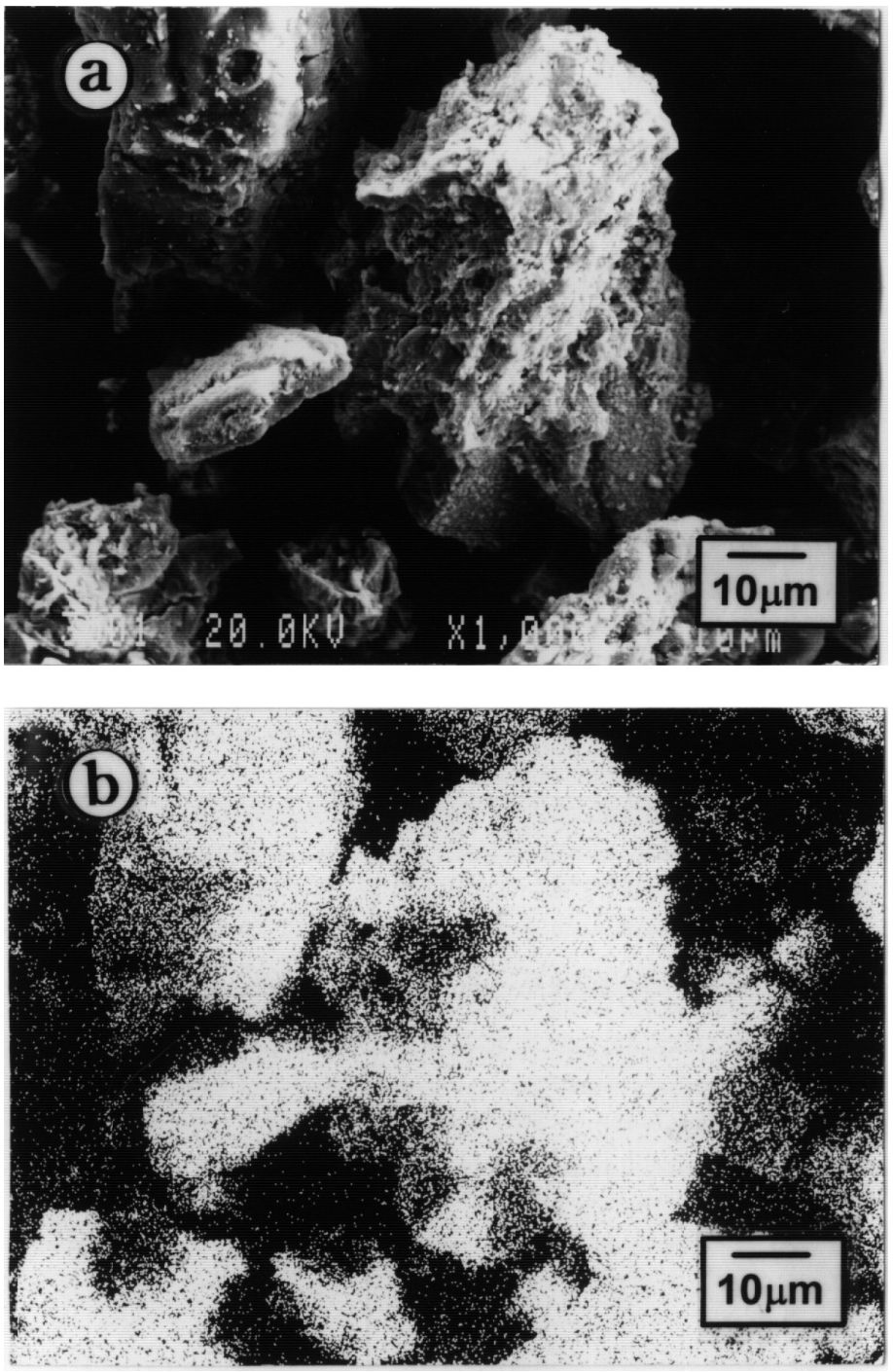

FIG. 10. Electron probe microanalysis of Mo_2N prepared from $H_3PMo_{12}O_{40} \cdot 26H_2O$: (a) SEM image of the area analyzed, (b) Mo distribution, and (c) P distribution.

N_2 and H_2 is initiated (Fig. 3b), especially for HPA. This demonstrates that NH_3 itself, not H_2 produced from it, is the true reducing agent. Furthermore, the difference in the NH_3 decomposition trace between HPA and MoO_3 indicates that NH_3 decomposition is an autocatalytic reaction in the present systems. In all cases, there is no significant contribution of P in the reduction process as evidenced by the small difference in the reduction behaviors between MoO_3 and $MoO_3 + P_2O_5$ (Fig. 3).

The N_2 BET measurements show that Mo_2N derived from HPA possesses a much lower specific surface area S_g as shown in Table 1. On the other hand, X-ray line

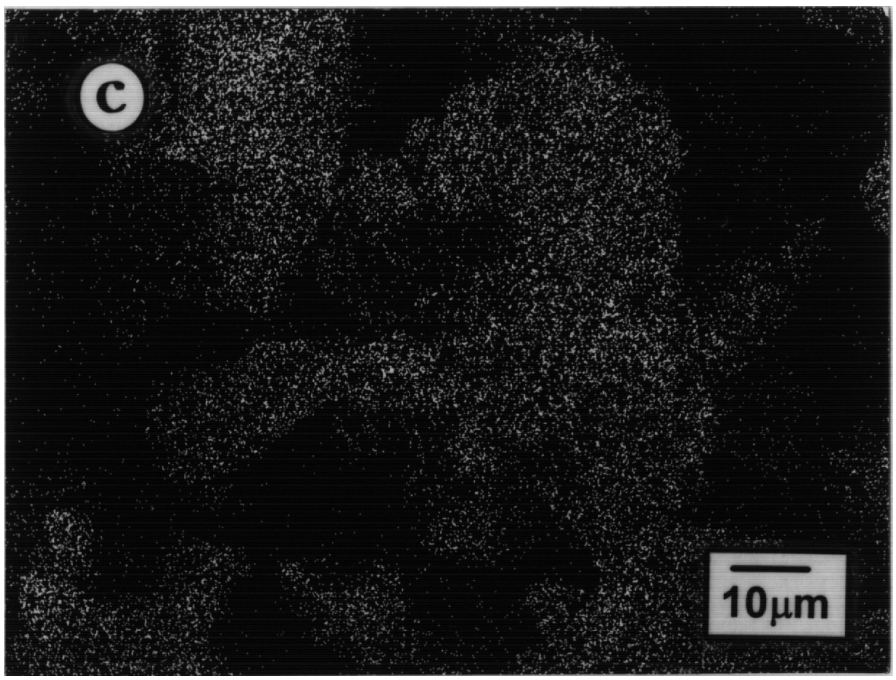

FIG. 10—*Continued*

broadening shows that much smaller Mo_2N particles are formed when HPA is employed as a precursor. Mo_2N prepared from $MoO_3 + P_2O_5$ also shows a lower S_g although its crystallite size determined by XRD is almost the same as that of MoO_3-derived Mo_2N. Thus it appears that P present in Mo_2N lowers the surface area, probably by pore blocking. Furthermore, CO chemisorption by Mo_2N was greatly reduced when the precursor contained P. The reduced amount of adsorbed CO is much lower than would be expected from the lower surface area, reflecting greatly reduced site densities. Thus, the surface of Mo_2N produced from $MoO_3 + P_2O_5$ or HPA is mostly covered by phosphorus which inhibits CO adsorption. Both of these effects, pore and site blocking are more serious for HPA-derived Mo_2N, probably because of more uniform P distribution compared to Mo_2N prepared from $MoO_3 + P_2O_5$ as discussed below.

Heteropolyacids contain heteroatoms which, in the present case, are P. They are retained in the product Mo_2N without any significant loss during preparation (Table 3). As discussed already, P mixed with MoO_3 does not affect the reduction and nitride formation process of MoO_3. It is plausible to assume that P contained in HPA would not have exerted a significant influence on the same process of HPA. Yet, P certainly had a marked effect on surface area and CO chemisorption of Mo_2N. Hence, it is interesting to compare the chemical state and the distribution of P in Mo_2N produced from HPA with Mo_2N produced from $MoO_3 + P_2O_5$.

XPS spectra in Fig. 11 indicate that the chemical state of P contained on the surface of Mo_2N produced from both HPA and $MoO_3 + P_2O_5$ is very similar to that of the precursor HPA. The spectra are characterized by the major peak at the binding energy of 133.5–133.8 eV which is interpreted as P bonded to metal. The species bonded to oxygen with a binding energy of 135.2 eV (25) is the other species. Thus, most of the P_2O_5 added to MoO_3 must have been reduced during the nitride preparation. The distribution of P in Mo_2N could be seen in Figs. 9 and 10 (EPMA) and in Table 3. The distribution is remarkably uniform for Mo_2N produced from HPA as demonstrated by EPMA in Fig. 10 and by the same value of P concentration demonstrated by XPS analysis (Table 3) for HPA precursor and Mo_2N prepared from it. The former indicates the lateral distribution of P while the latter represents the distribution along the depth of a Mo_2N particle. In Mo_2N produced from $MoO_3 + P_2O_5$, the lateral distribution is not as good, and more P is concentrated near the surface compared to HPA-derived Mo_2N. A large portion of P in this sample appears to have been segregated out of the pores of Mo_2N to the external surface and may form discrete particles. In this case, the blocking of pores and CO chemisorption sites of Mo_2N would become less effective. In any case, the different P distribution may affect the catalytic properties of Mo_2N which are the subjects of a forthcoming publication.

CONCLUSIONS

Mo_2N containing P was produced from a temperature-programmed reaction between $H_3PMo_{12}O_{40} \cdot 26H_2O$ and NH_3. Its morphology was different from that of Mo_2N

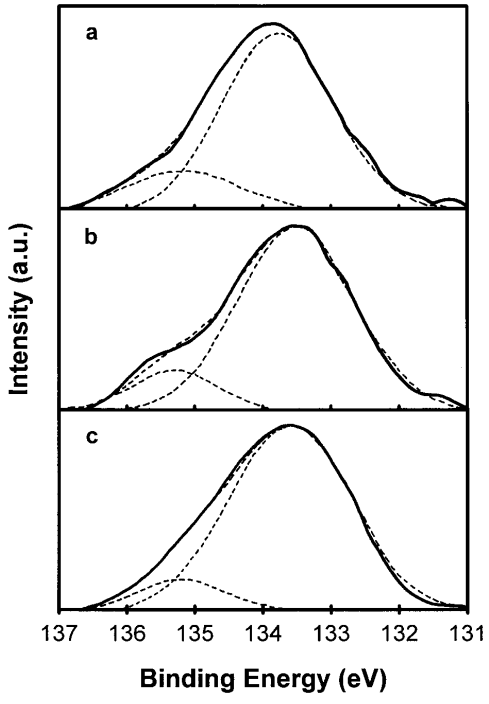

FIG. 11. XPS spectra of P contained in (a) $H_3PMo_{12}O_{40} \cdot 26H_2O$, (b) Mo_2N prepared from $H_3PMo_{12}O_{40} \cdot 26H_2O$, and (c) Mo_2N prepared from $MoO_3 + P_2O_5$. Curve fittings indicate that there exist two components for all spectra (area% in the parenthesis): (a) 135.2 eV (15.3%) and 133.8 eV (84.7%), (b) 135.3 eV (14.8%) and 133.5 eV (85.2%), and (c) 135.2% (8.5%) and 133.7 eV (91.5%).

produced from MoO_3. The reduction of HPA takes place at much lower temperatures than that required for the reduction of MoO_3 probably because of the enhanced diffusion rate of oxygen from HPA compared with that from MoO_3. Smaller Mo_2N particles were formed from HPA, yet the specific surface area and CO chemisorption were lower because of pore and site blocking by P. The distribution of P in Mo_2N was highly uniform. Similar results were obtained from temperature-programmed reaction between HPA and CH_4/H_2 to prepare Mo_2C.

REFERENCES

1. Bridgewater, A. J., Burch, R., and Michell, P. C. H., *J. Catal.* **78**, 116 (1982).
2. Kojima, I., and Miyazaki, E., *J. Catal.* **89**, 168 (1984).
3. Logan, M., Gellman, A., and Somorjai, G. A., *J. Catal.* **94**, 60 (1985).
4. Dun, J. W., Gulari, E., and Ng, K. Y. S., *Appl. Catal.* **15**, 247 (1985).
5. Leary, K. J., Michaels, J. N., and Stacy, A. M., *J. Catal.* **101**, 301 (1986).
6. Lee, J. S., Yeom, M. H., Park, K. Y., Nam, I., Chung, J. S., Kim, Y. G., and Moon, S. H., *J. Catal.* **128**, 126 (1991).
7. Lee, J. S., Yeom, M. H., and Lee, D. S., *J. Mol. Catal.* **62**, L45 (1990).
8. Volpe, L., and Boudart, M., *J. Phys. Chem.* **90**, 4878 (1986).
9. Bridgewater, A. J., Burch, R., and Mitchell, P. C. H., *J. Chem. Soc. Faraday Trans. 1* **76**, 1811 (1980).
10. Iglesia, E., Ribeiro, F. H., Boudart, M., and Baumgartner, J. E., *Catalysis Today* **15**, 307 (1992).
11. Lee, J. S., Locatelli, S., Oyama, S. T., and Boudart, M., *J. Catal.* **125**, 157 (1990).
12. Leclercq, L., Imura, K., Yoshida, S., Barbee, T., and Boudart, M., *in* "Preparation of Catalysts II" (B. Delmon, P. Grange, P. A. Jacobs, and G. Poncelet, Eds.), p. 627. Elsevier, Amsterdam, 1978.
13. Boudart, M., and Levy, R., *Science* **181**, 547 (1973).
14. Oyama, S. T., *Catalysis Today* **15**, 79 (1992).
15. Volpe, L., and Boudart, M., *J. Solid State Chem.* **59**, 332 (1985).
16. Volpe, L., and Boudart, M., *J. Solid State Chem.* **59**, 348 (1985).
17. Lee, J. S., Volpe, L., Ribeiro, F. H., and Boudart, M., *J. Catal.* **112**, 44 (1988).
18. Volpe, L., and Boudart, M., *Catal. Rev. Sci. Eng.* **27**, 515 (1985).
19. Lewis, J. M., and Kydd, R. A., *J. Catal.* **136**, 478 (1992).
20. Reyes, J. C., Avalos-Borja, M., Cordero, R. L., and Agudo, A. L., *Appl. Catal. A* **120**, 147 (1992).
21. Eijsbouts, S., van Gestel, J. N. M., van Veen, J. A. R., de Beer, V. H. J., and Prins, R., *J. Catal.* **131**, 412 (1991).
22. Lee, J. S., Oyama, S. T., and Boudart, M., *J. Catal.* **106**, 125 (1987).
23. Jeffery, G. H., Basset, J., Mendham, J., and Denny, R. C., *in* "Vogel's Textbook of Quantitative Chemical Analysis," 5th ed., p. 485. Longman Scientific, Essex, UK, 1989.
24. Misono, M., Okuhara, T., and Mizuno, N., *in* "Successful Design of Catalysts," p. 267. Elsevier, Amsterdam, 1988.
25. Moulder, J. F., Stickle, W. F., Sobol, P. E., and Bomben, K.D., "Handbook of X-Ray Photoelectron Spectroscopy," p. 233. Perkin–Elmer, Eden Prairie, MN, 1992.
26. Warren, B. F., "X-Ray Diffraction." Addison–Wesley, Reading, MA, 1969.